PROCEEDINGS A

royalsocietypublishing.org/journal/rspa

Research

Cite this article: Fatehiboroujeni S, Petra N, Goyal S. 2020 Linearized Bayesian inference for Young's modulus parameter field in an elastic model of slender structures. *Proc. R. Soc. A* **476**: 20190476.
http://dx.doi.org/10.1098/rspa.2019.0476

Received: 28 July 2019
Accepted: 13 May 2020

Subject Areas:
mechanical engineering, computational mathematics, biomechanics

Keywords:
slender structures, linear elasticity, inverse problems, adjoint-based methods, Bayesian inference, uncertainty qualification

Author for correspondence:
Soheil Fatehiboroujeni
e-mail: sfatehiboroujeni@ucmerced.edu

Linearized Bayesian inference for Young's modulus parameter field in an elastic model of slender structures

Soheil Fatehiboroujeni[1], Noemi Petra[2] and Sachin Goyal[1,3]

[1]Department of Mechanical Engineering, [2]Department of Applied Mathematics, and [3]Health Science Research Institute, University of California Merced, Merced, CA, USA

SF, 0000-0002-5129-7428

The deformations of several slender structures at nano-scale are conceivably sensitive to their non-homogenous elasticity. Owing to their small scale, it is not feasible to discern their elasticity parameter fields accurately using observations from physical experiments. Molecular dynamics simulations can provide an alternative or additional source of data. However, the challenges still lie in developing computationally efficient and robust methods to solve inverse problems to infer the elasticity parameter field from the deformations. In this paper, we formulate an inverse problem governed by a linear elastic model in a Bayesian inference framework. To make the problem tractable, we use a Gaussian approximation of the posterior probability distribution that results from the Bayesian solution of the inverse problem of inferring Young's modulus parameter fields from available data. The performance of the computational framework is demonstrated using two representative loading scenarios, one involving cantilever bending and the other involving stretching of a helical rod (an intrinsically curved structure). The results show that smoothly varying parameter fields can be reconstructed satisfactorily from noisy data. We also quantify the uncertainty in the inferred parameters and discuss the effect of the quality of the data on the reconstructions.

THE ROYAL SOCIETY PUBLISHING

© 2020 The Author(s) Published by the Royal Society. All rights reserved.

1. Introduction

The mechanics of deformable solids is governed by three sets of equations, namely the equations of equilibrium, compatibility conditions and constitutive laws. The constitutive laws describe the elasticity of material and capture the restoring effects of internal stresses on the deformation (or strains) [1]. Of the three sets of equations, only the constitutive law varies from material to material and needs to be identified by measurements. Identifying elasticity parameters of the constitutive law from noisy measurements of deformation field (or other directly observable quantities) presents several mathematical challenges in the field of inverse methods that are reviewed in [2,3]. These inverse methods leverage the other two sets of equations—equilibrium and compatibility—to discern the elasticity parameters from the observable data [4].

More recently, the need to formulate and solve inverse problems to identify elasticity parameters has extended beyond engineering problems to several biomechanical problems too [5–9]. For example, identifying the elasticity of tissues from their medical imaging helps detect certain illnesses [5]. For non-invasive characterization of biological materials via medical imaging, the inverse method described in [7–9] estimates their elastic properties by using finite element formulation of steady-state dynamic response of deformable solids immersed in fluids.

This paper particularly targets inverse elasticity problems involving slender structures, which are ubiquitous in nature. Continuum mechanics-based models of slender structures [10,11] are being increasingly employed to simulate the deformations of nano-scale biological filaments [12–14] (e.g. microtubules [15,16], DNA molecule [17,18], flagella or cila [19] and several others [20–22]), soft and active filaments [23,24], silver nano-wires [25] and carbon nano-tubes (CNTs) [26]. Many of these slender structures have non-homogenous elasticity, which may strongly influence the dynamics of their functionally relevant deformations such as looping in DNA [27]. The non-homogeneity in their constitutive law originates from their heterogenous atomistic structure. For example, in the case of DNA, the chemical sequence of different base-pair units along its length, which is primarily attributed to the genetic code, also dictates the variation of the constitutive law along the filament (referred to as secondary layer of code [28]), and thus governs its mechanical deformability.

However, at such small length scales, the identification of non-homogenous elasticity parameter field to date is not feasible from experimental measurements alone because physical experiments provide very limited information at that scale. For example, single-molecule experiments that use magnetic or optical tweezers to measure or prescribe the dynamics of micron-size beads attached to filaments such as microtubules [29] or DNA [30,31] provide data to estimate flexural and torsional rigidities averaged over their entire lengths [32–34], but not their variation along the length. Thermal fluctuations and imaging techniques also provide data to estimate only the average flexural rigidity; for example, refer to [35,36] in the context of actin filaments or microtubules. Likewise, atomic force microscopy can provide data to identify homogenous elasticity of silver nano-wires [25]. For identifying non-homogenous elasticity from experiments, perhaps the most useful information will be available from a futuristic imaging technique that attempts to observe dynamically deforming filaments at sufficiently high space and time resolutions [37,38]. In the case of DNA, thoughtfully designed cyclization experiments [39,40] together with a non-homogeneous rod model are also useful to identify the base-pair sequence-dependent constitutive law. Molecular dynamics (MD) simulations provide another option to generate informative data taking into account the atomistic structure that can be used with inverse methods to identify the constitutive law [41]. For example, in the context of nano-scale filaments, Kumar *et al*. [42] have shown how MD simulations may be used with Cauchy–Born rule to identify the constitutive law of nano-rods. Continuum modelling of CNTs from MD data and its successful prediction of experimentally observed shapes [43] presents a promising example of how informative MD data can be used for identifying elasticity parameters.

The variety of research efforts described above have spurred the need for development of systematic and robust methods in the inverse elasticity problems of slender structures. For example, Hinkle *et al*. [44] developed an inverse rod model to identify homogeneous constitutive laws of filaments from their deformations in cantilever equilibria. The cantilever equilibria are solved as an initial-value problem in the state-space form [45], which provide a framework for developing robust state estimation techniques and input reconstruction methods for the underlying inverse problem [46]. The possibility of extending this approach to use data from dynamic equilibria was explored by Gray *et al*. [47]. The inverse elasticity problems in the context of cantilevers are relevant to other applications as well. For instance, Barcilon [48] focuses on finding the flexural rigidity of cantilevers from vibration data for geo-physical applications. Such inverse problems of beams have also been considered for applications involving non-destructive testing by accounting for the limited measurements possible at the domain boundaries [49].

Inverse elasticity problems inherently tend to have several computational challenges stemming from the quality of data, and the large-scale nature of the unknown parameters (stemming from discretization). In this paper, we formulate two simple but representative inverse elasticity problems governed by the linear elastic equation with non-homogeneous coefficient field. In particular, we discuss the inversion of Young's modulus parameter field from synthetic observations of the displacement field under two loading scenarios: (i) cantilever bending and (ii) stretching of a helical elastic rod. Helical rods have relevance to several applications, such as [50–52] and require modelling intrinsic or stress-free curvature. To also quantify the uncertainties in our reconstruction, we formulate the inverse problem in a Bayesian inference framework. There is a wide range of literature on Bayesian inference applied to a variety of applications, for example we refer to [53–55] and citations therein.

To compute the solution of a Bayesian inverse problem (i.e. the posterior probability density) can become prohibitive, due to the expense of solving the forward model and the high dimensionality of the uncertain parameters (which are discretizations of Young's modulus field). To cope with the infinite-dimensional (i.e. large-scale) character of the parameter field, it is common to construct a Gaussian approximation to the posterior at the maximum *a posteriori* probability (MAP) point (see [56] and references therein). The MAP point in the Gaussian case coincides with the mean and it is given by the solution of the deterministic inverse elasticity problem. In this paper, we extend our previous work [57] where we solved the underlying least-squares minimization problem using an adjoint-based inexact Newton-conjugate gradient method, which uses first and second derivative information of the least-squares cost functional. The posterior covariance matrix (of the Gaussian approximation of the posterior) can be computed using the inverse of the Hessian of the least-squares cost functional of the deterministic inverse elasticity problem. We apply this method to quantify uncertainties in the inference of Young's modulus parameter field from synthetic observations of the deformation field in the cantilever and in the helical rod. In a deterministic setting, we have previously reported [57] results that show that the reconstructions of Young's modulus converge to the exact parameter as the observation error decreases. In the same paper, we have also shown that the number of Newton iterations is insensitive to the dimension of the parameters, i.e. the computational cost of solving the inverse problem stays constant as the size of the problem is increased. Therefore, the computational framework we propose for inverse elasticity problems has the potential to solve high-dimensional inverse elasticity problems that are of practical interest, such as those discussed above.

The paper is organized as follows. Section 2 introduces the forward linear elastic problem governing the mechanics of two-dimensional cantilevers or three-dimensional helical rods. Section 3 presents the inverse elasticity problem constrained by the linear elastic partial differential equation (PDE) formulated in a Bayesian framework. In §4, we present two model problems with smooth non-homogeneity in the elastic coefficient field and discuss the quality of the reconstructions of Young's modulus field and quantify the uncertainties in these reconstructions. We also discuss the quality of the data across the domain. Finally, §5 provides concluding remarks.

2. Forward problem: linear elastic model

The theory of elasticity models deformable bodies in the continuum limit. We model the mechanical deformation and stress distribution of deformable bodies using the balance of linear momentum [1] that states that

$$-\nabla \cdot \boldsymbol{\sigma}_{\boldsymbol{u}} = \boldsymbol{f}, \tag{2.1a}$$

where $\boldsymbol{\sigma}_{\boldsymbol{u}}$ denotes the stress tensor and the body force is denoted by $\boldsymbol{f}$. We employ a constitutive law that relates the stress tensor $\boldsymbol{\sigma}_{\boldsymbol{u}}$ and the strain tensor $\boldsymbol{\varepsilon}_{\boldsymbol{u}} = \frac{1}{2}(\nabla \boldsymbol{u} + \nabla \boldsymbol{u}^T)$ by

$$\boldsymbol{\sigma}_{\boldsymbol{u}} = \frac{\exp(E)}{1+\nu}\boldsymbol{\varepsilon}_{\boldsymbol{u}} + \frac{\exp(E)\nu}{(1+\nu)(1-2\nu)} tr(\boldsymbol{\varepsilon}_{\boldsymbol{u}})\boldsymbol{I}, \tag{2.1b}$$

where $\boldsymbol{u}$ is the displacement, $\exp(E)$ is Young's modulus, ν is Poisson's ratio, and $\boldsymbol{I}$ is the second-order unit tensor. We use the exponential form, $\exp(E)$ to define Young's modulus in order to ensure the positivity of this parameter as will be discussed further in the paper.

In this paper, we assume a model domain represented by Ω with boundary $\Gamma_D \cup \Gamma_N$, such that $\Gamma_D \cap \Gamma_N = \emptyset$. On Γ_D we impose the Dirichlet boundary condition, while on Γ_N a traction-free (i.e. Neumann) boundary condition, namely

$$\boldsymbol{u} = \boldsymbol{0} \quad \text{on } \Gamma_D \tag{2.1c}$$

and

$$\boldsymbol{\sigma}_{\boldsymbol{u}}\boldsymbol{n} = \boldsymbol{0} \quad \text{on } \Gamma_N. \tag{2.1d}$$

Here $\boldsymbol{n}$ is the outward normal vector. We note that the boundary value problem (2.1*a–d*) is the Navier–Lamé model of linear elasticity that describes the deformation of a body given by Ω (e.g. cantilever) [1].

The numerical solution of the boundary value problem (2.1*a–d*) can be obtained via the finite-element method [58], which requires the derivation of the so-called weak form of (2.1). This weak form is obtained by multiplying (2.1*a*) with a test function $\boldsymbol{v}$ from $V_d = \{\boldsymbol{v} = [v_1, v_2, v_3] \in H^1(\Omega) \times H^1(\Omega) \times H^1(\Omega) : \boldsymbol{v} = [0,0,0] \text{ in } \Gamma_D\}$ combined with Green's second identity [58]. This reads: Find $\boldsymbol{u} \in V_d$ such that

$$\int_\Omega \boldsymbol{\sigma}_{\boldsymbol{u}} : \boldsymbol{\varepsilon}_{\boldsymbol{v}} \, \mathrm{d}x = \int_\Omega \boldsymbol{f} \cdot \boldsymbol{v} \, \mathrm{d}x, \quad \forall \boldsymbol{v} \in V_d. \tag{2.2}$$

3. Inverse problem: Bayesian inversion for Young's modulus parameter field for a linear elastic model

The mechanical properties of a linearly elastic material, which can be described by Young's modulus $\exp(E)$ and Poisson's ratio ν parameters, cannot be directly observed or measured in an experiment hence these are typically unknown or uncertain. However, in experimental techniques—such as elastography [59]—it is common to measure the components of the displacement field across the domain, which can be used to infer these parameters. Inferring the mechanical properties of a material using the measurements, such as the displacement field $\boldsymbol{u}^{\text{obs}}$, can be formulated as an inverse problem. In this section, we formulate an inverse problem for the elasticity parameter field E, and describe an efficient numerical technique to solve the resulting optimization problem. In addition, to answer the question of what confidence we have in the inverse solution we turn to the framework of Bayesian inference [53,55]. In this framework, the inverse problem is formulated as a problem of statistical inference over the space of uncertain parameters. The solution is the posterior probability distribution function that expresses how likely it is that a set of candidate parameters gives rise to the observed data via the physical model. To find the posterior distribution $\pi_{\text{post}}(E|\boldsymbol{u}^{\text{obs}})$, i.e. the probability of parameter field E given the

observed data $\boldsymbol{u}^{\text{obs}}$, we rely on Bayes' theorem that combines the prior probability distribution, $\pi_{\text{prior}}(E)$, with a likelihood, $\pi_{\text{like}}(\boldsymbol{u}^{\text{obs}}|E)$, namely

$$\pi_{\text{post}}(E|\boldsymbol{u}^{\text{obs}}) \propto \pi_{\text{prior}}(E)\pi_{\text{like}}(\boldsymbol{u}^{\text{obs}}|E). \tag{3.1}$$

The prior captures any knowledge, information or assumption about the parameter field E, and the likelihood encodes the probability of observing data $\boldsymbol{u}^{\text{obs}}$, given a parameter field E. In this work, we use an additive Gaussian noise model that gives

$$\boldsymbol{u}^{\text{obs}} = \boldsymbol{F}(E) + \boldsymbol{\eta}, \quad \boldsymbol{\eta} \sim \mathcal{N}(\mathbf{0}, \Gamma_{\text{noise}}), \tag{3.2}$$

where $\Gamma_{\text{noise}} \in \mathbb{R}^{q\times q}$ is the measurement noise covariance matrix, q represents the number of observation points, and $\boldsymbol{F}(\cdot)$ is the parameter-to-observable operator that maps model parameters E to observable $\boldsymbol{u}$. Here, evaluation of this map requires solution of the Navier–Lamé PDE problem (2.1). To extract the observation points we apply the observation operator B. Furthermore, since the noise $\boldsymbol{\eta}$ is independent of E, thus $\boldsymbol{u}^{\text{obs}}|E \sim \mathcal{N}(\boldsymbol{F}(E), \Gamma_{\text{noise}})$, the likelihood is given by

$$\pi_{\text{like}}(\boldsymbol{u}^{\text{obs}}|E) \propto \exp\Big(-\frac{1}{2}\Big\langle B\boldsymbol{F}(E) - \boldsymbol{u}^{\text{obs}}, \Gamma_{\text{noise}}^{-1}(B\boldsymbol{F}(E) - \boldsymbol{u}^{\text{obs}})\Big\rangle\Big), \tag{3.3}$$

where $\langle\cdot,\cdot\rangle$ represents the L^2 inner product. We use a Gaussian prior defined by the mean E_{pr} and the covariance Γ_{pr} where we define the covariance as the inverse of the square of a Laplacian-like operator, namely $\Gamma_{\text{pr}} = (-\gamma\boldsymbol{\Delta}E + \delta E)^{-2}$ as in [56]. The parameters γ and δ control the correlation length and the variance of the prior operator and $\boldsymbol{\Delta}$ represents the Laplacian differential operator. We note that in finite dimensions the square root of the Γ_{pr}^{-1} becomes $\gamma K + \delta M$ where K is a stiffness matrix and M is a mass matrix [60–63]. The prior can therefore be written as

$$\pi_{\text{prior}}(E) \propto \exp\Big(-\frac{1}{2}\Big\langle E - E_{\text{pr}}, \Gamma_{\text{pr}}^{-1}(E - E_{\text{pr}})\Big\rangle\Big). \tag{3.4}$$

Assuming Gaussian noise and prior, using Bayes' theorem the posterior is given by [53,55]

$$\pi_{\text{post}}(E) \propto \exp\Big(-\frac{1}{2}\Big\langle B\boldsymbol{F}(E) - \boldsymbol{u}^{\text{obs}}, \Gamma_{\text{noise}}^{-1}(B\boldsymbol{F}(E) - \boldsymbol{u}^{\text{obs}})\Big\rangle - \frac{1}{2}\Big\langle E - E_{\text{pr}}, \Gamma_{\text{pr}}^{-1}(E - E_{\text{pr}})\Big\rangle\Big). \tag{3.5}$$

We note that if the parameter-to-observable map is linear the posterior probability density is Gaussian. In general however this is not the case. To cope with the large-scale character of the parameter field, it is common to construct a Gaussian approximation of the posterior at the MAP point (see [56], and references therein). This MAP point is the parameter vector maximizing the posterior (3.5). It can be found by minimizing the negative log of (3.5), which amounts to solving the optimization problem

$$\boldsymbol{E}_{\text{MAP}} = \arg\min_{E} \mathcal{J}(E) := -\log \pi_{\text{post}}(E). \tag{3.6}$$

Various optimization methods can be used to solve (3.6), e.g. gradient-based methods such as steepest descent or nonlinear conjugate gradient, or second derivative-based (i.e. Hessian) methods [64,65]. For an efficient computation of the MAP point, here we use adjoints- and Hessian-based methods, as we will show in the next section. One of the advantages in doing so, besides the fast convergence of second derivative-based methods, is that the posterior covariance matrix Γ_{post} of the Gaussian approximation can then be obtained by computing the action of the inverse of the Hessian (of $\mathcal{J}$ at E_{MAP}) on vectors [53,55], and the cost of such action is only two linear(ized) PDE solves.

To ensure that Young's modulus is positive, we use the parametrization $\exp(E)$ for the inversion [56]. Alternatively, one can impose bound constraints (for example combined with the maximum entropy principle [66–69]) to construct probability distributions that exclude negative values of the inversion parameter. By using a Gaussian prior our method remains versatile for various inverse problems that involve parameters such as Poisson's ratio [70,71] or those in coupled [26] or nonlinear (softening-hardening) forms of constitutive law [72] and allows us to achieve scalability with respect to the size of inversion parameter space. To mitigate the influence

of using a Gaussian prior, we use a large variance for the prior and let the observation data inform the posterior.

(a) Calculating the MAP points: adjoint-based inexact Gauss–Newton-CG

To solve (3.6) efficiently, here we focus on the Gauss–Newton method, which is known to converge fast [64,65]. Starting with an initial guess for the parameter E, Newton's method iteratively updates this field by $E^{k+1} = E^k + \alpha \hat{E}^k$, where E^k is the current parameter and the Newton direction $\hat{E}^k$ is obtained by solving the linear system

$$\mathcal{H}(E^k)\hat{E}^k = -\mathcal{G}(E^k). \tag{3.7}$$

Here, $\mathcal{G}$ is the gradient of the objective functional $\mathcal{J}$ in (3.6), and $\mathcal{H}$ is its Hessian operator. To guarantee convergence, the new value of the parameter is found by damping the Newton direction, i.e. by choosing a step length α via an Armijo line search for example, such that the cost functional in (3.6) sufficiently decreases at each iteration [64,65].

To derive the gradient and Hessian-vector product, we use the Lagrangian formalism [73–75], in which the Lagrange multiplier function $\boldsymbol{p} \in V_d$ takes the role of the test function in enforcing the weak form of the elastic problem (2.2). The Lagrangian functional is given by

$$\mathscr{L}(\boldsymbol{u}, E, \boldsymbol{p}) = \mathscr{J}(E) + \langle \boldsymbol{\sigma}_{\boldsymbol{u}}, \boldsymbol{\varepsilon}_{\boldsymbol{p}} \rangle - \langle \boldsymbol{f}, \boldsymbol{p} \rangle. \tag{3.8}$$

The gradient of $\mathcal{J}$ can be found as the variation of the Lagrangian $\mathcal{L}$ with respect to E, provided variations of $\mathscr{L}$ with respect to $\boldsymbol{u}$ and $\boldsymbol{p}$ vanish. Thus, the gradient $\mathcal{G}(E)$ is found by taking the Fréchet derivative of the Lagrangian functional in the directions $\tilde{\boldsymbol{p}}$, $\tilde{\boldsymbol{u}}$ and $\tilde{E}$ and is shown with $\mathcal{L}_{\boldsymbol{p}}$, $\mathcal{L}_{\boldsymbol{u}}$ and $\mathcal{L}_E$, respectively

$$\langle \boldsymbol{\sigma}_{\boldsymbol{u}}, \boldsymbol{\epsilon}_{\tilde{\boldsymbol{p}}} \rangle - \langle \boldsymbol{f}, \tilde{\boldsymbol{p}} \rangle = \mathcal{L}_{\boldsymbol{p}} \tilde{\boldsymbol{p}}, \tag{3.9a}$$

$$\langle \boldsymbol{\sigma}_{\tilde{\boldsymbol{u}}}, \boldsymbol{\epsilon}_{\boldsymbol{p}} \rangle + \left\langle B^* \Gamma_{\text{noise}}^{-1} (B\boldsymbol{u} - \boldsymbol{u}^{\text{obs}}), \tilde{\boldsymbol{u}} \right\rangle = \mathcal{L}_{\boldsymbol{u}} \tilde{\boldsymbol{u}} \tag{3.9b}$$

and

$$\left\langle \Gamma_{\text{pr}}^{-1}(E - E_{\text{pr}}), \tilde{E} \right\rangle + \left\langle \frac{\tilde{E}\ \exp(E)}{1+\nu} \boldsymbol{\varepsilon}_{\boldsymbol{u}}, \boldsymbol{\varepsilon}_{\boldsymbol{p}} \right\rangle + \left\langle \frac{\tilde{E}\ \exp(E)\nu}{(1+\nu)(1-2\nu)} tr(\boldsymbol{\varepsilon}_{\boldsymbol{u}})\boldsymbol{I}, \boldsymbol{\varepsilon}_{\boldsymbol{p}} \right\rangle = \mathcal{L}_E \tilde{E}, \tag{3.9c}$$

where B^* is the adjoint of the observation operator, B. We note that the left-hand side of (3.9*a*) is the weak form of the underlying forward problem, and the left-hand side of (3.9*b*) represents the weak form of the corresponding adjoint equation, which is obtained by invoking the stationary of $\mathscr{L}$ with respect to the forward variable $\boldsymbol{u}$ (or $\mathcal{L}_{\boldsymbol{u}} = 0$). The strong form (obtained by integration by parts) of the adjoint equation reads

$$-\nabla \cdot \boldsymbol{\sigma}_{\boldsymbol{p}} = -B^* \Gamma_{\text{noise}}^{-1} (B\boldsymbol{u} - \boldsymbol{u}^{\text{obs}}) \quad \text{in } \Omega, \tag{3.10a}$$

$$\boldsymbol{p} = \boldsymbol{0} \quad \text{on } \Gamma_D \tag{3.10b}$$

and

$$\boldsymbol{\sigma}_{\boldsymbol{p}} \boldsymbol{n} = \boldsymbol{0} \quad \text{on } \Gamma_N. \tag{3.10c}$$

We note that, as expected, the adjoint equation is driven by the negative misfit between the solution $\boldsymbol{u}$ of the forward problem and the observational data $\boldsymbol{u}^{\text{obs}}$.

Once we have $\boldsymbol{u}$ and $\boldsymbol{p}$, we can evaluate the gradient, which is given in the left-hand side of (3.9*c*). To enforce the stationary of the gradient (or $\mathcal{L}_E = 0$) we use Newton's method, as explained above, where to compute the direction $\hat{E}^k$ we solve equation (3.7). The action of the

Hessian operator $\mathcal{H}(E^k)$ in a direction $\hat{E}^k$ is obtained by taking second variations of $\mathcal{L}$ with respect to all variables [76,77]. This can be expressed as

$$\langle \boldsymbol{\sigma}_{\hat{\boldsymbol{u}}}, \boldsymbol{\epsilon}_{\tilde{\boldsymbol{p}}} \rangle = \mathcal{L}_{\boldsymbol{p}\boldsymbol{u}} \hat{\boldsymbol{u}}, \tag{3.11a}$$

$$\left\langle B^* \Gamma_{\text{noise}}^{-1} B\hat{\boldsymbol{u}}, \tilde{\boldsymbol{u}} \right\rangle = \mathcal{L}_{\boldsymbol{u}\boldsymbol{u}} \hat{\boldsymbol{u}}, \tag{3.11b}$$

$$\left\langle \frac{\tilde{E}\ \exp(E)}{1+\nu} \boldsymbol{\epsilon}_{\hat{\boldsymbol{u}}}, \boldsymbol{\varepsilon}_{\boldsymbol{p}} \right\rangle + \left\langle \frac{\tilde{E}\ \exp(E)\nu}{(1+\nu)(1-2\nu)} tr(\boldsymbol{\epsilon}_{\hat{\boldsymbol{u}}}) \boldsymbol{I}, \boldsymbol{\varepsilon}_{\boldsymbol{p}} \right\rangle = \mathcal{L}_{E\boldsymbol{u}} \hat{\boldsymbol{u}}, \tag{3.11c}$$

$$0 = \mathcal{L}_{\boldsymbol{p}\boldsymbol{p}} \hat{\boldsymbol{p}}, \tag{3.12a}$$

$$\left\langle \boldsymbol{\sigma}_{\tilde{\boldsymbol{u}}}, \boldsymbol{\epsilon}_{\hat{\boldsymbol{p}}} \right\rangle = \mathcal{L}_{\boldsymbol{u}\boldsymbol{p}} \hat{\boldsymbol{p}}, \tag{3.12b}$$

$$\left\langle \frac{\tilde{E}\ \exp(E)}{1+\nu} \boldsymbol{\varepsilon}_{\boldsymbol{u}}, \boldsymbol{\epsilon}_{\hat{\boldsymbol{p}}} \right\rangle + \left\langle \frac{\tilde{E}\ \exp(E)\nu}{(1+\nu)(1-2\nu)} tr(\boldsymbol{\varepsilon}_{\boldsymbol{u}}) \boldsymbol{I}, \boldsymbol{\epsilon}_{\hat{\boldsymbol{p}}} \right\rangle = \mathcal{L}_{E\boldsymbol{p}} \hat{\boldsymbol{p}}, \tag{3.12c}$$

$$\left\langle \frac{\hat{E}\ \exp(E)}{1+\nu} \boldsymbol{\varepsilon}_{\boldsymbol{u}}, \boldsymbol{\epsilon}_{\tilde{\boldsymbol{p}}} \right\rangle + \left\langle \frac{\hat{E}\ \exp(E)\nu}{(1+\nu)(1-2\nu)} tr(\boldsymbol{\varepsilon}_{\boldsymbol{u}}) \boldsymbol{I}, \boldsymbol{\epsilon}_{\tilde{\boldsymbol{p}}} \right\rangle = \mathcal{L}_{p E} \hat{E}, \tag{3.13a}$$

$$\left\langle \frac{\hat{E}\ \exp(E)}{1+\nu} \boldsymbol{\epsilon}_{\tilde{\boldsymbol{u}}}, \boldsymbol{\varepsilon}_{\boldsymbol{p}} \right\rangle + \left\langle \frac{\hat{E}\ \exp(E)\nu}{(1+\nu)(1-2\nu)} tr(\boldsymbol{\epsilon}_{\tilde{\boldsymbol{u}}}) \boldsymbol{I}, \boldsymbol{\varepsilon}_{\boldsymbol{p}} \right\rangle = \mathcal{L}_{\boldsymbol{u}E} \hat{E}, \tag{3.13b}$$

$$\left\langle \hat{E}, \Gamma_{\text{pr}}^{-1} \tilde{E} \right\rangle + \left\langle \frac{\tilde{E}\,\hat{E}\ \exp(E)}{1+\nu} \boldsymbol{\varepsilon}_{\boldsymbol{u}}, \boldsymbol{\varepsilon}_{\boldsymbol{p}} \right\rangle + \left\langle \frac{\tilde{E}\,\hat{E}\ \exp(E)\nu}{(1+\nu)(1-2\nu)} tr(\boldsymbol{\varepsilon}_{\boldsymbol{u}}) \boldsymbol{I}, \boldsymbol{\varepsilon}_{\boldsymbol{p}} \right\rangle = \mathcal{L}_{EE} \hat{E}. \tag{3.13c}$$

Equations (3.11)–(3.13) sequentially represent the derivatives of equation (3.9) with respect to $\boldsymbol{u}, \boldsymbol{p}$ and E. With some abuse of notation, the above system can be summarized as

$$\mathscr{H} \begin{bmatrix} \hat{\boldsymbol{u}} \\ \hat{E} \\ \hat{\boldsymbol{p}} \end{bmatrix} = \begin{bmatrix} \mathscr{L}_{\boldsymbol{u}\boldsymbol{u}} & \mathscr{L}_{\boldsymbol{u}E} & \mathscr{L}_{\boldsymbol{u}\boldsymbol{p}} \\ \mathscr{L}_{E\boldsymbol{u}} & \mathscr{L}_{EE} & \mathscr{L}_{E\boldsymbol{p}} \\ \mathscr{L}_{\boldsymbol{p}\boldsymbol{u}} & \mathscr{L}_{\boldsymbol{p}E} & \mathscr{L}_{\boldsymbol{p}\boldsymbol{p}} \end{bmatrix} \begin{bmatrix} \hat{\boldsymbol{u}} \\ \hat{E} \\ \hat{\boldsymbol{p}} \end{bmatrix} = \begin{bmatrix} -\mathscr{L}_{\boldsymbol{u}} \\ -\mathscr{L}_{E} \\ -\mathscr{L}_{\boldsymbol{p}} \end{bmatrix}. \tag{3.14}$$

To solve the above system, we assume that u and p satisfy the state and the adjoint equations such that $\mathscr{L}_{\boldsymbol{u}} = \mathscr{L}_{\boldsymbol{p}} = 0$. Then by using block elimination we arrive at the so-called *incremental forward problem* (derived from the third row of equation (3.14)), which in strong form reads

$$-\boldsymbol{\nabla} \cdot \boldsymbol{\sigma}_{\hat{\boldsymbol{u}}} = -\boldsymbol{\nabla} \cdot \left(\frac{\hat{E}\ \exp(E)}{1+\nu} \boldsymbol{\varepsilon}_{\boldsymbol{u}} + \frac{\hat{E}\ \exp(E)\nu}{(1+\nu)(1-2\nu)} tr(\boldsymbol{\varepsilon}_{\boldsymbol{u}}) \boldsymbol{I} \right) \quad \text{in } \Omega, \tag{3.15a}$$

$$\hat{\boldsymbol{u}} = \boldsymbol{0} \quad \text{on } \Gamma_D, \tag{3.15b}$$

$$\boldsymbol{\sigma}_{\hat{\boldsymbol{u}}} \boldsymbol{n} = \boldsymbol{0} \quad \text{on } \Gamma_N, \tag{3.15c}$$

and the *incremental adjoint problem* (derived from the first row of equation (3.14)), which in strong form reads

$$-\boldsymbol{\nabla} \cdot \boldsymbol{\sigma}_{\hat{\boldsymbol{p}}} = -B^* \Gamma_{\text{noise}}^{-1} B\hat{\boldsymbol{u}} \quad \text{in } \Omega, \tag{3.16a}$$

$$\hat{\boldsymbol{p}} = \boldsymbol{0} \quad \text{on } \Gamma_D, \tag{3.16b}$$

$$\boldsymbol{\sigma}_{\hat{\boldsymbol{p}}} \boldsymbol{n} = \boldsymbol{0} \quad \text{on } \Gamma_N. \tag{3.16c}$$

For a discussion on practical implementation of the Gauss–Newton-CG optimization method in finite dimensions, we refer the reader to the technical report [77].

4. Results

This section presents two model problems to illustrate the performance of the inverse method described in §3. The first problem focuses on the inversion of a smoothly non-homogenous Young's modulus field for planar bending of a cantilever beam. The second problem targets the same inversion parameter but for a three-dimensional helical structure. The observation data $\boldsymbol{u}^{\text{obs}}$ are synthesized by solving the forward problem described in §2 and adding a noise level of 1% to the solution. In other words, the signal-to-noise ratio is equal to 100. For both numerical studies, we consider measurement points everywhere in the domain (i.e. these are taken at all discretization points). In what follows, the traction $\boldsymbol{t}$ on the boundary Γ_N is zero, and we consider a nonzero body force $\boldsymbol{f}$ to be applied on the structure.

To solve the inverse problems, we used hIPPYlib [63,78], an inverse problem python-based library. This library contains scalable algorithms for PDE-based deterministic and Bayesian inverse problems. It builds on FEniCS [79,80] for the discretization of the PDEs and on PETSc [81] for scalable and efficient linear algebra operations and solvers needed for the solution of the PDEs. An online repository is also made publicly available that entails the python scripts as well as the mesh files for the following simulations [82].

In a previous work [57], we demonstrated the scalability of the computational framework (in a deterministic setting), which shows that the computational cost does not scale with the mesh size. We measure this cost in terms of the number of PDE solves required for the algorithm to converge to a given tolerance. Here we stop the optimization iterations when the norm of the gradient at the current iteration compared with the norm of the initial gradient falls below 10^{-9}. With this criteria, the planar bending scenario presented in the following section requires 35 PDE solves, and the helical rod scenario that follows next requires 161.

(a) Planar bending of a cantilever beam

The domain $\Omega = [0, 8] \times [0, 0.5]$ for this model problem is a two-dimensional rectangular section of a cantilever (as shown in figure 1). The boundary conditions are the following. On the left boundary, Γ_D, we impose a homogeneous Dirichlet condition to model a clamped end, and on Γ_N we impose a traction-free, i.e. homogeneous Neumann boundary condition. The goal of this model problem is to identify Young's modulus parameter field when Poisson's ratio ν is known (here taken as 0.25). The synthetic observation data $\boldsymbol{u}^{\text{obs}}$ for the inversion of E is obtained by simulating the cantilever bending subject to uniform body force $\boldsymbol{f} = (0, 6.5 \times 10^{-3})$ and with a 'true' parameter field

$$E_{\text{true}} = 3.0 - \sin\left[\pi\left(\frac{x}{8} - \frac{1}{2}\right)\right]. \tag{4.1}$$

The prior is chosen as follows. The prior mean is chosen to be zero and the prior covariance matrix is constructed by using the inverse of a Laplacian-like operator, as explained in §3. For the cantilever bending example, the parameter γ, which controls the smoothness of the parameter field E, has a constant value 0.4, and δ is also chosen to be constant 0.1. We choose these values so that the prior distribution is not too rough over the domain, yet has a large enough measure of uncertainty everywhere. For a more systematic approach for selection of γ and δ see [83,84]. A one-dimensional representation (at $y = 0.25$ m) of the prior mean, standard deviation and samples from the Gaussian prior distribution are illustrated in figure 2*a*.

Figure 3 shows the synthetic observation data $\boldsymbol{u}^{\text{obs}}$, the 'true' state variable, $\boldsymbol{u}^{\text{true}}$, obtained with the true (proposed) parameter field, and the recovered state solution $\boldsymbol{u}^{\text{MAP}}$ obtained with the inversion result along the bending neutral axis of the beam (i.e. $y = 0$). This figure shows that the difference (i.e. the misfit) between $\boldsymbol{u}^{\text{MAP}}$ and $\boldsymbol{u}$ is larger towards the right side of the beam.

In figure 4, we compare the variance of the prior with that of the posterior. This result shows that the variance is reduced, which can be attributed to the information gained from the data in solving the inverse problem. We note however that improvement in the variance of the posterior

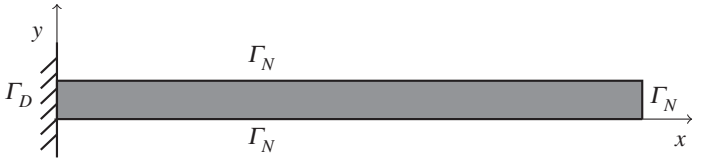

Figure 1. The domain Ω (grey shaded region) and coordinate system for the linear elastic problem (2.1) modelling a cantilever. The boundary $\partial\Omega = \Gamma_N \cup \Gamma_D$ (with $\Gamma_N \cap \Gamma_D = \emptyset$), where Γ_N and Γ_D are boundaries with Dirichlet and Neumann boundary conditions, respectively, defined in (2.1*c*–*d*).

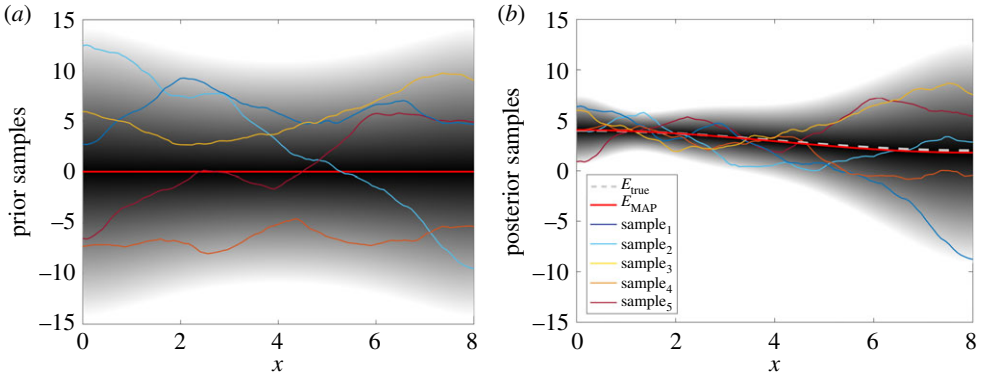

Figure 2. The one-dimensional representation (at $y = 0.25$ m) of the marginals of the prior (*a*) and the posterior (*b*) probability distributions, with higher probability density indicated by darker shading. The grey shaded area corresponds to a 95% confidence interval. The prior mean and the MAP point are shown in solid red (the thickest solid curve) and the samples from the prior and the posterior are shown in various colours. (Online version in colour.)

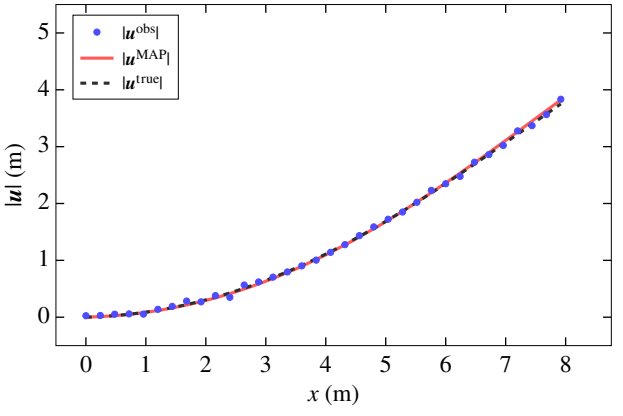

Figure 3. The synthetic observation $\boldsymbol{u}^{\text{obs}}$ (blue dots), state variable, $\boldsymbol{u}^{\text{true}}$, obtained with the true (proposed) parameter field, and the solution of the forward problem (black dashed line), and $\boldsymbol{u}^{\text{MAP}}$, obtained with the inversion results (red solid line) shown along the bending neutral axis of the beam (i.e. at $y = 0$). (Online version in colour.)

is reduced as we move toward the free end (right end) of the cantilever. This is because the dependence of the deformation field on E is captured by the constitutive law, implying that the higher the stress and strain the more sensitive the solution of the elastic problem is to E. In the cantilever loading scenario, bending curvature and therefore the stress and strain decrease as we move from the clamped end (left) to the free end (right). Consequently, the sensitivity of the deformation field to the parameter (E) diminishes toward the free end, and therefore the data becomes increasingly less informative in that region. Furthermore, since the sensitivity depends

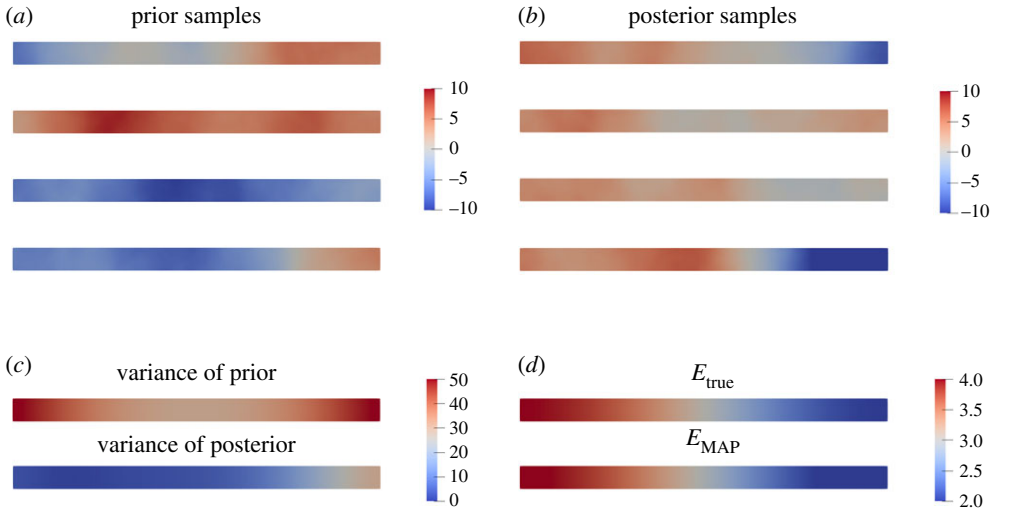

Figure 4. Several realizations of the prior (*a*) and posterior (*b*) using a colour scale. The variance σ^2 of the prior and posterior (*c*). MAP points versus true parameter field (*d*). (Online version in colour.)

on strain, and in turn on the gradient of the deformation field, at the clamped end the variance of the posterior is still slightly larger than what one would expect from the above argument, due to the boundary effect on the gradient information.

(b) Stretching of a helical spring

In this section, we define a model problem for the identification of the elastic properties of a more realistic rod, namely of the helical proteins (sheath) that play a key role in the genome injection mechanism of the bacteriophage T4 virus [85]. The helical sheath proteins on the viral tail are stretched before injection. When the virus attaches to a target cell, the elastic energy of the helical proteins is used to inject the DNA into the target cell. Continuum rod theory is shown to be capable of capturing the important features of this mechanism [85], however the accuracy of continuum modelling is strictly determined by accurate knowledge of the constitutive law. The methodology presented here can be used not only to estimate the constitutive law of such structures, but also to quantify the degree of uncertainty in the estimations. The problem presented in this section shows how the constitutive law of a helical rod can be estimated using the measurements of the displacement field.

The Poisson ratio ν in this model problem is constant, e.g. $\nu = 0.25$, and the sinusoidal Young's modulus, E, is given by

$$E_{\text{true}} = 3.0 - \sin\left[\pi\left(\frac{x}{20} - \frac{1}{2}\right)\right]. \tag{4.2}$$

The geometry for this problem is a helix with radius $R = 1$ mm and pitch $P = 2$ mm as shown in figure 5. The synthetic observations $\boldsymbol{u}^{\text{obs}}$ for this case are generated by stretching the helical structure under a uniform body force $\boldsymbol{f} = (2.2 \times 10^{-3}, 0, 0)$. In this example, the parameter γ has a constant value 1.0, and δ is also chosen to be constant 0.1.

In figure 6, we show the variance and samples from the prior and posterior probability distributions. The results show that the variance of the posterior is smaller than that of the prior, which is due to the information we learned from the observations. However, toward the free end of the structure (right-hand side in figure 5) as the stress and strain decline to zero, the data is not informative for accurate identification of the parameter field, therefore the posterior shows a larger variance in this region.

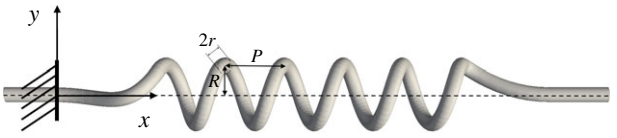

Figure 5. The domain of the linear elastic problem modelling a helical rod. The radius of the helix is $R = 1$ mm and its pitch $P = 2$ mm. The overall length of the structure is $L = 20$ mm shown with a dashed line and the cross-section of the rod is a circle with radius $r = 0.25$ mm.

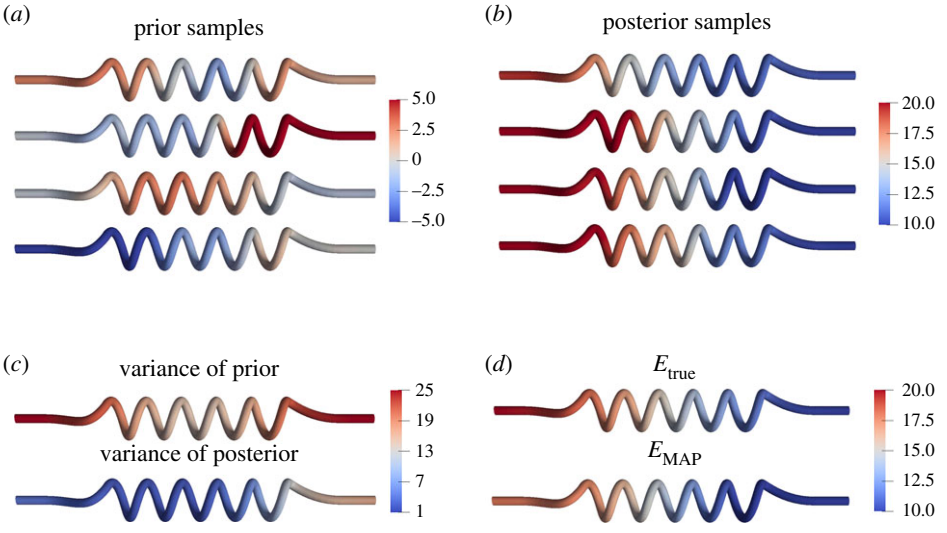

Figure 6. Samples of the prior (*a*) and of the posterior (*b*). The variance of the prior and the posterior (*c*). True parameter field and the MAP points (*d*). The difference between the prior and posterior samples reflects the information gained from the observational data. (Online version in colour.)

5. Discussion and conclusion

This paper presents a Bayesian inversion approach to estimate Young's modulus parameter field in an elastic model of slender structures. To illustrate the performance of the inverse method, we formulated two model problems, one employing planar bending of a cantilever beam and the other employing stretching of a helical spring. Our observation data are synthetic measurement of the deformation field obtained by solving the forward problem and adding noise to the data.

We compute the inverse solution via an inexact Gauss–Newton-CG method and quantify the uncertainties in the reconstruction via a Bayesian framework. The inversion results closely reconstruct Young's modulus field with low uncertainties in parts of the domain undergoing high stress and strain. Reconstructions deteriorate, i.e. the uncertainties increase in parts of the domain subject to low stress and strain, implying low sensitivity of the observable data to the inversion parameter.

The results in this paper employ synthetic observations on two simple model problems to study the performance of the proposed method. As a part of our future work, we intend to apply this inversion approach to realistic applications, such as uncertainty quantification of the constitutive law parameters for microtubules and nano-wires using MD simulations and data obtained from physical experiments. In real applications depending on the availability of the measurements, the observation data can be in both static or dynamic equilibrium. Moreover, for nano-scale filaments such as DNA, the effect of thermal fluctuations in the observation data, on

one hand introduces uncertainty in the data and, on the other hand, provides information by itself on the deformability of the filaments. Finally, future developments should consider nonlinearity in the constitutive laws without any *a priori* assumption on its form. This necessitates formulating a computationally efficient forward model that can simulate the deformations with any user-specified nonlinear constitutive law [51]. Therefore, the inverse models for nonlinear constitutive laws have to evolve together with the development of corresponding forward models.

Data accessibility. This article has no additional data.

Authors' contributions. All authors helped to conceive, design and coordinate the study and helped draft the manuscript. All authors gave final approval for publication and agree to be held accountable for the work performed therein.

Competing interests. We declare we have no competing interests.

Funding. No funding has been received for this article.

Acknowledgements. N.P. acknowledges support from the National Science Foundation (NSF) via grant nos. SI2-SSI ACI-1550547 and CAREER-1654311.

References

1. Gurtin ME. 2003 *An introduction to continuum mechanics*. Boston, MA: Academic Press.
2. Bonnet M, Constantinescu A. 2005 Inverse problems in elasticity. *Inverse Prob.* **21**, R1. (doi:10.1088/0266-5611/21/2/R01)
3. Avril S *et al.* 2008 Overview of identification methods of mechanical parameters based on full-field measurements. *Exp. Mech.* **48**, 381–402. (doi:10.1007/s11340-008-9148-y)
4. Constantinescu A. 1995 On the identification of elastic moduli from displacement-force boundary measurements. *Inverse Probl. Eng.* **1**, 293–313. (doi:10.1080/174159795088027587)
5. Doyley MM. 2012 Model-based elastography: a survey of approaches to the inverse elasticity problem. *Phys. Med. Biol.* **57**, R35. (doi:10.1088/0031-9155/57/3/R35)
6. Heyden S, Nagler A, Bertoglio C, Biehler J, Gee MW, Wall WA, Ortiz M. 2015 Material modeling of cardiac valve tissue: experiments, constitutive analysis and numerical investigation. *J. Biomech.* **48**, 4287–4296. (doi:10.1016/j.jbiomech.2015.10.043)
7. Brigham JC, Aquino W, Mitri FG, Greenleaf JF, Fatemi M. 2007 Inverse estimation of viscoelastic material properties for solids immersed in fluids using vibroacoustic techniques. *J. Appl. Phys.* **101**, 023509. (doi:10.1063/1.2423227)
8. Rosario DE, Brigham JC, Aquino W. 2008 Identification of material properties of orthotropic elastic cylinders immersed in fluid using vibroacoustic techniques. *Ultrasonics* **48**, 547–552. Selected Papers from {ICU} 2007. (doi:10.1016/j.ultras.2008.07.004)
9. Aguilo MA, Aquino W, Brigham JC, Fatemi M. 2010 An inverse problem approach for elasticity imaging through vibroacoustics. *IEEE Trans. Med. Imaging* **29**, 1012–1021. (doi:10.1109/TMI.2009.2039225)
10. Goyal S, Perkins NC, Lee CL. 2005 Nonlinear dynamics and loop formation in kirchhoff rods with implications to the mechanics of DNA and cables. *J. Comput. Phys.* **209**, 371–389. (doi:10.1016/j.jcp.2005.03.027)
11. Simo JC, Marsden JE, Krishnaprasad PS. 1988 The Hamiltonian structure of nonlinear elasticity: the material and convective representations of solids, rods, and plates. *Arch. Ration. Mech. Anal.* **104**, 125–183. (doi:10.1007/BF00251673)
12. Neukirch S, van der Heijden G. 2002 Geometry and mechanics of uniform n-plies: from engineering ropes to biological filaments. *J. Elast.* **69**, 41–72. (doi:10.1023/A:1027390700610)
13. Hwang W. 2015 Biofilament dynamics: line-to-rod-level descriptions. In *Multiscale Modeling in Biomechanics and Mechanobiology* (eds S De, W Hwang, E Kuhl), pp. 63–83. London, UK: Springer.
14. Klapper I. 1996 Biological applications of the dynamics of twisted elastic rods. *J. Comput. Phys.* **125**, 325–337. (doi:10.1006/jcph.1996.0097)
15. Sept D, MacKintosh FC. 2010 Microtubule elasticity: connecting all-atom simulations with continuum mechanics. *Phys. Rev. Lett.* **104**, 018101. (doi:10.1103/PhysRevLett.104.018101)
16. Hawkins T, Mirigian M, Yasar MS, Ross JL. 2010 Mechanics of microtubules. *J. Biomech.* **43**, 23–30. Special Issue on Cell Mechanobiology. (doi:10.1016/j.jbiomech.2009.09.005)
17. Lillian TD, Goyal S, Kahn JD, Meyhöfer E, Perkins N. 2008 Computational analysis of looping of a large family of highly bent DNA by LacI. *Biophys. J.* **95**, 5832–5842. (doi:10.1529/biophysj.108.142471)

18. Hoffman KA. 2004 Methods for determining stability in continuum elastic-rod models of DNA. *Phil. Trans. R. Soc. A* **362**, 1301–1315. (doi:10.1098/rsta.2004.1382)
19. Hilfinger A, Chattopadhyay AK, Jülicher F. 2009 Nonlinear dynamics of cilia and flagella. *Phys. Rev. E* **79**, 051918. (doi:10.1103/PhysRevE.79.051918)
20. Qin Z, Buehler MJ, Kreplak L. 2010 A multi-scale approach to understand the mechanobiology of intermediate filaments. *J. Biomech.* **43**, 15–22. Special Issue on Cell Mechanobiology. (doi:10.1016/j.jbiomech.2009.09.004)
21. Goldstein RE, Goriely A. 2006 Dynamic buckling of morphoelastic filaments. *Phys. Rev. E* **74**, 010901. (doi:10.1103/PhysRevE.74.010901)
22. Odijk T. 1998 Microfibrillar buckling within fibers under compression. *J. Chem. Phys.* **108**, 6923–6928. (doi:10.1063/1.476107)
23. Gazzola M, Dudte LH, McCormick AG, Mahadevan L. 2018 Forward and inverse problems in the mechanics of soft filaments. *Open Sci.* **5**, 171628. (doi:10.1098/rsos.171628)
24. Fatehiboroujeni S, Gopinath A, Goyal S. 2018 Nonlinear oscillations induced by follower forces in prestressed clamped rods subjected to drag. *J. Comput. Nonlinear Dyn.* **13**, 121 005–121 008. (doi:10.1115/1.4041681)
25. Chen Y, Dorgan BL, McIlroy DN, Eric Aston D. 2006 On the importance of boundary conditions on nanomechanical bending behavior and elastic modulus determination of silver nanowires. *J. Appl. Phys.* **100**, 104301. (doi:10.1063/1.2382265)
26. Kumar A, Mukherjee S, Paci JT, Chandraseker K, Schatz GC. 2011 A rod model for three dimensional deformations of single-walled carbon nanotubes. *Int. J. Solids Struct.* **48**, 2849–2858. (doi:10.1016/j.ijsolstr.2011.06.004)
27. Goyal S, Perkins N. 2008 Looping mechanics of rods and DNA with non-homogeneous and discontinuous stiffness. *Int. J. Non-Linear Mech.* **44**, 1121–1129. (doi:10.1016/j.ijnonlinmec.2008.06.013)
28. Geggier S, Vologodskii A. 2010 Sequence dependence of DNA bending rigidity. *Proc. Natl Acad. Sci. USA* **107**, 15 421–15 426. (doi:10.1073/pnas.1004809107)
29. Kikumoto M, Kurachi M, Tosa V, Tashiro H. 2006 Flexural rigidity of individual microtubules measured by a buckling force with optical traps. *Biophys. J.* **90**, 1687–1696. (doi:10.1529/biophysj.104.055483)
30. Smith SB, Finzi L, Bustamante C. 1992 Direct mechanical measurements of the elasticity of single DNA molecules by using magnetic beads. *Science* **258**, 1122–1126. (doi:10.1126/science.1439819)
31. Deufel C, Forth S, Simmons CR, Dejgosha S, Wang MD. 2007 Nanofabricated quartz cylinders for angular trapping: DNA supercoiling torque detection. *Nat. Methods* **4**, 223–225. (doi:10.1038/nmeth1013)
32. Baumann CG, Smith SB, Bloomfield VA, Bustamante C. 1997 Ionic effects on the elasticity of single DNA molecules. *Proc. Natl Acad. Sci. USA* **94**, 6185–6190. (doi:10.1073/pnas.94.12.6185)
33. Hagerman PJ. 1988 Flexibility of DNA. *Annu. Rev. Biophys. Biophys. Chem.* **17**, 265–286. (doi:10.1146/annurev.bb.17.060188.001405)
34. Strick TR, Allemand JF, Bensimon D, Bensimon A, Croquette V. 1996 The elasticity of a single supercoiled DNA molecule. *Science* **271**, 1835–1837. (doi:10.1126/science.271.5257.1835)
35. Gittes F, Mickey B, Nettleton J, Howard J. 1993 Flexural rigidity of microtubules and actin filaments measured from thermal fluctuations in shape. *J. Cell Biol.* **120**, 923–934. (doi:10.1083/jcb.120.4.923)
36. Käs J, Strey H, Sackmann E. 1994 Direct imaging of reptation for semiflexible actin filaments. *Nature* **368**, 226–229. (doi:10.1038/368226a0)
37. Snoeyink C, Wereley S. 2013 A novel 3D3C particle tracking method suitable for microfluidic flow measurements. *Exp. Fluids* **54**, 1453. (doi:10.1007/s00348-012-1453-7)
38. Snoeyink C, Wereley S. 2012 Three-dimensional locating of paraxial point source with axicon. *Opt. Lett.* **37**, 2058–2060. (doi:10.1364/OL.37.002058)
39. Manning RS, Maddocks JH, Kahn JD. 1996 A continuum rod model of sequence-dependent DNA structure. *J. Chem. Phys.* **105**, 5626–5646. (doi:10.1063/1.472373)
40. Goyal S, Perkins NC, Meiners JC. 2008 Resolving the sequence-dependent stiffness of DNA using cyclization experiments and a computational rod model. *J. Comput. Nonlinear Dyn.* **3**, 011003. (doi:10.1115/1.2802582)
41. Ayton GSD, Bardenhagen S, McMurtry P, Sulsky D, Voth GA. 2001 Interfacing molecular dynamics with continuum dynamics in computer simulation: toward an application to biological membranes. *IBM J. Res. Dev.* **45**, 417–426. (doi:10.1147/rd.453.0417)

42. Kumar A, Kumar S, Gupta P. 2015 A helical Cauchy-Born rule for special cosserat rod modeling of nano and continuum rods. *J. Elast.* **124**, 81–106. (doi:10.1007/s10659-015-9562-1)
43. Pantano A, Parks DM, Boyce MC. 2004 Mechanics of deformation of single- and multi-wall carbon nanotubes. *J. Mech. Phys. Solids* **52**, 789–821. (doi:10.1016/j.jmps.2003.08.004)
44. Hinkle AR, Goyal S, Palanthandalam-Madapusi HJ. 2012 Constitutive-law modeling of microfilaments from their discrete-structure simulations—a method based on an inverse approach applied to a static rod model. *ASME J. Appl. Mech.* **79**, 051005. (doi:10.1115/1.4006449)
45. Anker N, Palanthandalam-Madapusi HJ. 2013 Solving for cantilever equilibria as initial value problems. *J. Mech. Med. Biol.* **13**, 1320001. (doi:10.1142/S0219519413200017)
46. Palanthandalam-Madapusi HJ, Goyal S. 2011 Robust estimation of nonlinear constitutive law from static equilibrium data for modeling the mechanics of DNA. *Automatica* **47**, 1175–1182. (doi:10.1016/j.automatica.2011.02.047)
47. Gray J, Fatehiboroujeni S, Goyal S. 2015 Robustness analysis of algorithms to estimate constitutive laws of biological filaments. In *ASME 2015 Int. Mechanical Engineering Congress & Exposition*, vol. 14: Emerging Technologies; Safety Engineering and Risk Analysis; Materials: Genetics to Structures. Houston, TX, USA, p. V014T11A006; 10 pages. American Society of Mechanical Engineers.
48. Barcilon V. 1982 Inverse problem for the vibrating beam in the free–clamped configuration. *Phil. Trans. R. Soc. Lond. A* **304**, 211–251. (doi:10.1098/rsta.1982.0012)
49. Lesnic D. 2016 Determination of the flexural rigidity of a beam from limited boundary measurements. *J. Appl. Math. Comput.* **20**, 17–34. (doi:10.1007/BF02831922)
50. Maghsoodi A, Chatterjee A, Andricioaei I, Perkins NC. 2017 Dynamic model exposes the energetics and dynamics of the injection machinery for bacteriophage T4. *Biophys. J.* **113**, 195–205. (doi:10.1016/j.bpj.2017.05.029)
51. Fatehiboroujeni S, Palanthandalam-Madapusi H, Goyal S. 2018 Computational rod model with user-defined nonlinear constitutive laws. *J. Comput. Nonlinear Dyn.* **13**, 101 006–101 008. (doi:10.1115/1.4041028)
52. Wolgemuth CW, Sun SX. 2006 Elasticity of α-helical coiled coils. *Phys. Rev. Lett.* **97**, 248101. (doi:10.1103/PhysRevLett.97.248101)
53. Tarantola A. 2005 *Inverse problem theory and methods for model parameter estimation*. Philadelphia, PA: SIAM.
54. Stuart AM. 2010 Inverse problems: a bayesian perspective. *Acta Numerica* **19**, 451–559. (doi:10.1017/S0962492910000061)
55. Kaipio J, Somersalo E. 2005 *Statistical and computational inverse problems*, vol. 164. Applied Mathematical Sciences. New York, NY: Springer.
56. Isaac T, Petra N, Stadler G, Ghattas O. 2015 Scalable and efficient algorithms for the propagation of uncertainty from data through inference to prediction for large-scale problems, with application to flow of the Antarctic ice sheet. *J. Comput. Phys.* **296**, 348–368. (doi:10.1016/j.jcp.2015.04.047)
57. Fatehiboroujeni S, Petra N, Goyal S. 2016 Towards adjoint-based inversion of the Lamé parameter field for slender structures with cantilever loading. In *ASME 2016 Int. Design Engineering Technical Conf. and Computers and Information in Engineering Conf.*, pp. V008T10A031–V008T10A031. American Society of Mechanical Engineers.
58. Gockenbach MS. 2006 *Understanding and implementing the finite element method*. Philadelphia, PA: Society for Industrial and Applied Mathematics (SIAM).
59. Oberai AA, Gokhale NH, Feijóo GR. 2003 Solution of inverse problems in elasticity imaging using the adjoint method. *Inverse Prob.* **19**, 297. (doi:10.1088/0266-5611/19/2/304)
60. Spantini A, Solonen A, Cui T, Martin J, Tenorio L, Marzouk Y. 2015 Optimal low-rank approximations of Bayesian linear inverse problems. *SIAM J. Sci. Comput.* **37**, A2451–A2487. (doi:10.1137/140977308)
61. Bui-Thanh T, Burstedde C, Ghattas O, Martin J, Stadler G, Wilcox LC. 2012 Extreme-scale UQ for Bayesian inverse problems governed by PDEs. In *SC12: Proc. of the Int. Conf. for High Performance Computing, Networking, Storage and Analysis 2012, Salt Lake City, UT*, pp. 1–11. (doi:10.1109/SC.2012.56)
62. Bui-Thanh T, Ghattas O, Martin J, Stadler G. 2013 A Computational framework for infinite-dimensional Bayesian inverse problems part I: the linearized case, with application to global seismic inversion. *SIAM J. Sci. Comput.* **35**, A2494–A2523. (doi:10.1137/12089586X)

63. Villa U, Petra N, Ghattas O. 2019 hIPPYlib: An Extensible Software Framework for Large-Scale Inverse Problems Governed by PDEs; Part I: Deterministic Inversion and Linearized Bayesian Inference. (https://arxiv.org/abs/1909.03948)
64. Nocedal J, Wright SJ. 2006 *Numerical optimization*, 2nd edn. Berlin, Germany: Springer.
65. Kelley CT. 1999 *Iterative methods for optimization*. Philadelphia, PA: SIAM.
66. Mihai LA, Woolley TE, Goriely A. 2018 Stochastic isotropic hyperelastic materials: constitutive calibration and model selection. *Proc. R. Soc. A* **474**, 20170858. (doi:10.1098/rspa.2017.0858)
67. Staber B, Guilleminot J. 2017 Stochastic hyperelastic constitutive laws and identification procedure for soft biological tissues with intrinsic variability. *J. Mech. Behav. Biomed. Mater.* **65**, 743–752. (doi:10.1016/j.jmbbm.2016.09.022)
68. Staber B, Guilleminot J. 2015 Stochastic modeling of a class of stored energy functions for incompressible hyperelastic materials with uncertainties. *C R Mécanique* **343**, 503–514. (doi:10.1016/j.crme.2015.07.008)
69. Staber B, Guilleminot J. 2018 A random field model for anisotropic strain energy functions and its application for uncertainty quantification in vascular mechanics. *Comput. Methods Appl. Mech. Eng.* **333**, 94–113. (doi:10.1016/j.cma.2018.01.001)
70. Lakes RS. 2017 Negative-Poisson's-Ratio materials: auxetic solids. *Annu. Rev. Mater. Res.* **47**, 63–81. (doi:10.1146/annurev-matsci-070616-124118)
71. Lakes R. 1993 Advances in negative Poisson's ratio materials. *Adv. Mater.* **5**, 293–296. (doi:10.1002/adma.19930050416)
72. OLIVER J. 1996 Modelling strong discontinuities in solid mechanics via strain softening constitutive equations. part 1: fundamentals. *Int. J. Numer. Methods Eng.* **39**, 3575–3600. (doi:10.1002/(SICI)1097-0207(19961115)39:21<3575::AID-NME65>3.0.CO;2-E)
73. Tröltzsch F. 2010 *Optimal control of partial differential equations: theory, methods and applications*, vol. 112. Graduate Studies in Mathematics. American Mathematical Society.
74. Hinze M, Pinnau R, Ulbrich M, Ulbrich S. 2009 *Optimization with PDE Constraints*. Berlin, Germany: Springer.
75. Borzì A, Schulz V. 2011 *Computational optimization of systems governed by partial differential equations*. Philadelphia, PA: Society for Industrial and Applied Mathematics.
76. Petra N, Zhu H, Stadler G, Hughes TJR, Ghattas O. 2012 An inexact Gauss–Newton method for inversion of basal sliding and rheology parameters in a nonlinear Stokes ice sheet model. *J. Glaciol.* **58**, 889–903. (doi:10.3189/2012JoG11J182)
77. Petra N, Stadler G. 2011 Model variational inverse problems governed by partial differential equations. Technical Report 11-05 The Institute for Computational Engineering and Sciences, The University of Texas at Austin.
78. Villa U, Petra N, Ghattas O. 2018 hIPPYlib: an extensible software framework for large-scale deterministic and Bayesian inverse problems. *J. Open Source Softw.* **3**, 940. (doi:10.21105/joss.00940)
79. Dupont T, Hoffman J, Johnson C, Kirby R, Larson M, Logg A, Scott R. 2003 The FEniCS project. Technical report.
80. Logg A, Mardal KA, Wells GN eds. 2012 *Automated solution of differential equations by the finite element method*, vol. 84. Lecture Notes in Computational Science and Engineering. Berlin, Germany: Springer.
81. Balay S, Buschelman K, Gropp WD, Kaushik D, Knepley M, McInnes LC, Smith BF, Zhang H. 2001 PETSc home page. See http://www.mcs.anl.gov/petsc.
82. Github repository of documents. See https://github.com/sfatehi/Bayesian-Inverse-Elasticity (accessed 18 March 2020).
83. Daon Y, Stadler G. 2018 Mitigating the influence of boundary conditions on covariance operators derived from elliptic PDEs. *Inverse Problems and Imaging* **12**, 1083–1102. (doi:10.3934/ipi.2018045)
84. Roininen L, Huttunen JMJ, Lasanen S. 2014 Whittle-Matérn priors for Bayesian statistical inversion with applications in electrical impedance tomography. *Inverse Problems & Imaging* **8**, 561. (doi:10.3934/ipi.2014.8.561)
85. Maghsoodi A, Chatterjee A, Andricioaei I, Perkins NC. 2016 A First model of the dynamics of the bacteriophage T4 injection machinery. *J. Comput. Nonlinear Dyn.* **11**, 041026. (doi:10.1115/1.4033554)